

Microimaging of hairless rat skin by magnetic resonance at 900 MHz[☆]

Rakesh Sharma*

CIMAR, National High Magnetic Field Laboratory, Florida State University, Tallahassee, FL 32310, USA

FAMU-FSU College of Engineering, Tallahassee, FL 32310, USA

Received 10 April 2008; accepted 30 June 2008

Abstract

Purpose: Quantitative imaging of the rat skin was performed using magnetic resonance imaging (MRI) at 900 MHz.

Materials and methods: A number of imaging techniques utilized for multiple contrast included magnetization transfer contrast, spin-lattice relaxation constant (T1-weighting), combination of T2-weighting with magnetic field inhomogeneity (T2*-weighting), magnetization transfer weighting and diffusion tensor weighting. These were used to obtain 2D slices and 3D multislice-multiecho images with high magnetic resonance contrast. These 2D and 3D imaging techniques were combined to achieve high-resolution MRI.

Results: Oil–water phantom showed distinct fat–water contrast. The dermis and epidermis, including the stratum corneum remnants, of nude rat skin were distinct due to their proton magnetic resonance as a result of proton interactions with the skin interstitial tissue. Combined details obtained from high-resolution, high-quality ex vivo skin images with different multicontrast characteristics generated better differentiation of skin layers, sublayers and significant correlation ($r^2=0.4927$ for MRI area, $r^2=0.3068$ for histology area; $P<0.0148$) of MR data with co-registered histological areas of the epidermis as well as the hair follicle.

Conclusion: The multiple contrast approach provided a noninvasive ex vivo MRI visualization with semi-quantitative assessment of the major skin structures including the stratum corneum remnants, epidermis, hair, papillary dermis, reticular dermis and hypodermis.

© 2009 Published by Elsevier Inc.

Keywords: Histology imaging; In vitro skin; Micro-MRI; Lipid; Ultrahigh resolution

1. Introduction

High-resolution magnetic resonance (MR) microimaging is emerging as a bioimaging research tool. The success depends on available magnet field strength to achieve high signal-to-noise ratio (SNR) at minimum inhomogeneity and increased pixel resolution in tissues. The scanner used at the National High Magnetic Field Laboratory (NHMFL) in Tallahassee, FL, was a 900-MHz ultra-wide bore magnetic resonance imaging (MRI) scanner (Bruker Biospin, Bellerika, MA, USA) with maximum field gradient amplitude (2.1 T/cm) equipped with the PARAVISION 3.2 software. It displays the temporal and spatial homogeneity of a phantom

object up to 1 part per billion in uniformity over a 4×1.5-cm cylindrical volume with ultrahigh-resolution MR microimaging capability [1]. It has advantages over other alternative skin fat imaging techniques in that it has the potential for both quantitative and noninvasive morphological 3D evaluation of the structures of the skin [2]. At 900-MHz or 21-T magnetic field, both contrast and resolution are likely enhanced up to 20 μm using thin slices with different contrast methods. However, the effects of high magnetic field and radio-frequency (RF) energy on tissues are not known [2].

1.1. Skin MRI imaging

Skin MRI microscopy is emerging as an evaluation tool of subdermal changes due to obesity, skin cancer, inflammation, radiation exposures, plastic surgery and allergic sensitivity. In clinical imaging, the main challenge is still how to distinguish different characteristics of skin components such as semisolid glycolipids, hair root, oil-rich sebaceous glands and active epidermis viable layer with

[☆] Grant support: National Science Foundation support for 900 MHz microimaging users' facility research fund.

* Center of Magnetic Resonance and Applied Research, National High Magnetic Field Laboratory, Florida State University, and B 222F, FAMU-FSU College of Engineering, Tallahassee, FL 32310, USA. Tel.: +1 850 264 8659
E-mail address: rsharma@eng.fsu.edu.

limited success using different clinical MRI techniques as listed in Table 1 [2–12].

Water-fat protons display distinct phase contrast, magnetization transfer contrast (MTC), specific relaxivities and chemical shift contrast in skin tissues. These useful tools and several contributory factors such as very small dimensions of skin components in the range of 500–1500 μm , dependence of hair keratin, oil- and fat-rich components on magnetization transfer property, longer imaging pulse sequences, etc., are reviewed in Table 1. However, poor spatial resolution and accurate quantitative *in vivo* 1.5-T measurements of skin features still remain as unsolved problems due to the short T2 characteristics of skin tissues and the multiexponential nature of skin T2 behavior [3–6,13–20]. For quantitative MRI of skin tissue, better visualization of skin structures may be achieved by high-resolution multicontrast MRI approach at 900 MHz. Furthermore, image processing of these images can extract out measurable skin structures for comparison with histology structures.

The purpose of the present study was to perform an exploratory microimaging study of *ex vivo* rat skin using a high field magnet. The fat MRI signal was more achievable at high magnetic field. The large SNR combined with small RF and gradient circuitry made possible the acquisition of high-resolution images. Data from different multiple MRI modalities are presented to provide a more comprehensive view of identifying multiple skin structures in the skin samples.

Table 1

Different techniques of *in vivo* skin MRI are shown with the techniques used and skin property measured at different magnetic field strengths using different clinical imagers

MRI technique used (visible skin structure)	Magnetic field used (T)	Reference
1. RF energy absorption (eye and ear)	21.5, 42, 56	[2]
2. Spin echo imaging (skin morphology and irritation)	1.5	[3]
3. Chemical shift microimaging (subcutaneous skin lesions)	11.7	[4]
4. Standard multislice imaging (MTC of skin fat)	1.5	[5]
5. Magnetization transfer contrast with periodic pulsed saturation (human skin)	1.5	[6]
6. Magnetization transfer imaging (field dispersion in water-macromolecular proton MT)	9.4	[7]
7. Short echo time MRI (visualization of the natural state of human stratum corneum water)	1.5	[8]
8. <i>In vivo</i> proton relaxation times analysis by MRI (skin layers)	1.5	[9]
9. <i>In vivo</i> high-resolution MRI (skin in a whole-body system)	1.5	[10]
10. <i>In vivo</i> MR microscopy by customized 3D gradient and partial flip-angle using spin-echo pulse sequences and very small transmit/receive coils (human skin structures)	1.5	[11]
11. Standard multislice imaging (MTC).	1.5	[12]

2. Materials and methods

2.1. Rat skin tissue preparation

Microimaging experiments were conducted at NHMFL (Tallahassee, FL, USA). For skin sample, normal healthy 3-week-old nude rats (Charles River Lab, Wilmington, MA, USA) were sacrificed by overdose of sodium pentobarbital anesthesia (60 mg/kg). Immediately, rat abdomen nude rat skin fresh samples (9 mm diameter) in phosphate buffer saline pH 7.4 were taken to the imaging suite, transported at 23°C from the lab of Dr. Mandip Sachdeva at Florida Agriculture and Mechanical University, Tallahassee, FL, to NHMFL. The rat skin sample was immediately held in place in 10-mm Wilmad NMR tube between two Teflon plugs inside phosphate buffer saline. The NMR tube with samples was placed in a RF coil insert, and MR imaging using a 900-MHz MRI microimager was performed according to the Animal Care University Center protocol at Florida State University, Tallahassee, FL. The experimental conditions were maintained at a temperature of 23°C and <50% relative humidity during sample handling through imaging the *ex vivo* skin samples. The skin holding Teflon assembly is shown in Fig. 1.

2.2. Nine hundred-megahertz MRI Instrument

MR microimaging was performed on a 900-MHz vertical-bore (106 mm internal bore diameter) superconducting magnet (Bruker Biospin, Bellerika, CA, USA) located at NHMFL with a customized imaging console (PARAVISION 3.2). A specialized RF coil insert was used (Fig. 1), consisting of a complete circular copper foil ring sitting on a half-circle copper foil ring separated by a thin sheet of mica (inner diameter 10 mm and outer diameter 25 mm). It maintains up to 90% coil filling factor and high SNR at low electrical resistance. The shield (upper layer) was used as a return path of the current flowing in the loop coil of the RF coil insert. Adjustment of the MRI slice position was carried out using a FLASH localizer image and a reproducible yellow color external landmark on the NMR tube holding the sample inside the RF coil as shown in Fig. 1.

2.3. Phantom imaging

Three different types of phantoms were used for validating fat-water contrast and establishing measurement accuracy. The phantoms were (1) oil–water phantom 4.5% (w/v) made of fractionated oat oil in ethanol (USP 6355693) for fat-water T2* MRI phase contrast comparable with skin lipids; (2) poly-L-lysine-coated alginate beads for achieving ultrahigh resolution; and (3) Teflon plastic object microimaging with minimum inhomogeneity and submillimeter dimensionality. Water in the tube was imaged by proton density imaging for calibration of proton MRI signal intensity as reference assuming a 55 M concentration. The scan parameters were set at NEX=2, slice number=10, slice thickness=0.4 mm.

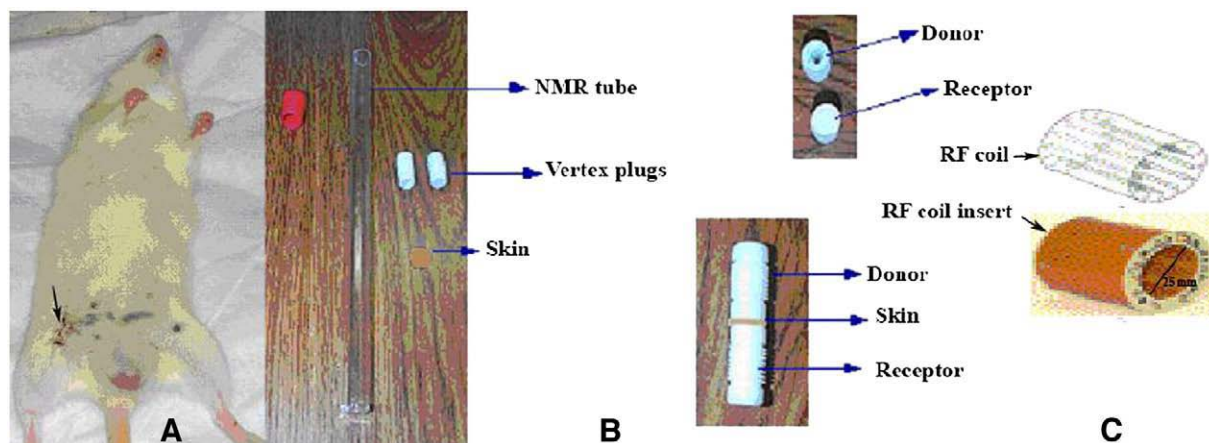


Fig. 1. A rat is shown with the site of the excised skin tissue for microimaging (Panel A). An assembly is shown to hold the rat skin sample to fit in a 10-mm NMR Wilmad tube in the 900-MHz MRI microimager (Panel B). The RF coil insert 25-mm imaging probe (Bruker Biospin) is shown with the NMR tube holding a skin sample for imaging (Panel C).

2.3.1. Oil–water phantom

The oil–water phantom had two tubes with oil in the outer tube (diameter 10 mm) and water inside the tube (diameter 6 mm) held in place in the 25-mm microimaging probe (Bruker-Biospin) inside the magnet bore to test the fat–water phase differences and to check data reproducibility.

The image contrast was measured due to the chemical shift between fat and water at different oil concentrations of 2–4.5% (w/v) in the oil–water phantom filled with oil and water. Gradient echo (GE) images were obtained with TR=700 ms, flip angle=25° and TE varying from 8 to 10 ms in steps of 0.3 ms to obtain in-phase and out-of-phase effects. The signal intensity was measured in the region of the oil/water interface in all images as earlier described [21,22].

2.3.2. Poly-L-lysine-coated alginate bead phantom

The 50-μm-sized beads were packed into a 5-mm-diameter NMR tube for microimaging using proton density-weighted imaging technique at TE=15 ms and TR=1500 ms to calibrate the spatial resolution.

2.3.3. Teflon object

A 1.0-mm Teflon object was placed in a 3-mm-wide NMR Wilmad tube for microimaging using proton density-weighted imaging technique at TE=15 ms and TR=1500 ms to establish measurement accuracy.

2.4. High magnetic field inhomogeneity and ultrahigh resolution

The high field magnet generates a high magnetization signal and increases spatial resolution. However, both the noise and bright spot inhomogeneity also increase at high magnetic field during short scan GE imaging techniques as shown in Eq. (1). These images multiplied with the signal modulator causing bright spot inhomogeneity and edge enhancement artifacts. Use of low-pass filtering and extrapolation of these images reduce both edge enhancement

and bright spot inhomogeneity. For this, sensitivity profile S calculation by gradient-weighted smoothing method is an ideal choice for adaptive smoothing using filtered gradient of the inhomogeneity in the images as the weight of smoothing. The inhomogeneity correction and denoising methods minimize inhomogeneity by gradient-based and entropy-based correction without loss of signal intensity as described elsewhere [23,24]. The magnet sensitivity profile S can be used to calculate inhomogeneity-corrected images by the following equation.

$$\tilde{I} = \frac{I}{S} \times \left\| \frac{S}{I} \right\|_2 \times \|I\|_2 \quad (1)$$

where S is the sensitivity profile, I is the original image with inhomogeneity and $\|S/I\|_2 \cdot \|I\|_2$ is the operator for Frobenius norm to correct the inhomogeneity in the image. The average pixel intensity in the image domain is retained after correction.

The inhomogeneity and higher noise due to ultrahigh magnetic field of 21 T were measured on gradient echo flow compensation (GEFC) images [23]. The local entropy minimization with a bicubic spline model (LEMS) corrects the intensity inhomogeneity of up to 80% that arises from the surface coil array. The denoising of images by gradient-based approach was reported using convolution with real value image phase in truncated k -space and inhomogeneity correction as shown in Eq. (1) [23,24]. In the present study, different rat skin structures were distinguished up to 15-μm ultrahigh resolution by the use of an ultrahigh magnetic field 900-MHz MR imager.

2.5. Rat skin study

Excised fresh rat skin samples held in place in 10-mm NMR tube were immersed in fomblin, which has no MR signal. These skin samples were imaged using 2D spin echo techniques for morphological evaluation and the 2D GE techniques for phase contrast evaluation. For

qualitative analysis, rat skin MR images were obtained using different contrast techniques as shown in Table 2. For morphological evaluation, different skin structures of epidermis, dermis, hair follicle and sebaceous glands were identified by multislice-multiecho spin echo technique. The GE images at TR=700 ms and TE=8 and 10 ms were obtained in a short period of 1–2 min [25]. The signal intensities were measured in different rat skin regions including the epidermis, dermis, hair follicles and sebaceous gland.

Images for maximum visualization of skin structures were obtained using six different MRI contrast techniques of T1-weighting, T2-weighting, Dixon chemical shift weighted, DTI-weighting and MTC weighting. The T₂*-weighted GE-FC technique was used for rapid imaging [25].

2.6. Multiple contrast approach

In the present study, combined multiple-contrast imaging approach was used to enhance the SNR, resolution and contrast of measurable skin lipids with viable epidermis at minimum inhomogeneity. The assumption was that all skin components are visible by use of one or another contrast weighting scheme. T1-weighted, T2*-weighted, MTC-weighted, diffusion tensor imaging (DTI)-weighted and fat-water contrast enhancement techniques comprised the multiple contrast approach. A combination of different T1, T2, proton density, MTC, DTI-weighted and GEFC techniques was used to achieve contrast specific to each skin structure. These weighting schemes with optimized parameter settings (TE and TR for T1, T2 and proton density; B1 offset and strength for MTC; *b* values and directions for DTI) are shown in Table 2, adopted from the

fitting procedures suggested in the Bruker Biospin PARAVISION 3.2 protocols [25].

2.7. Resolution

The pixel (in plane) resolution was field-of-view (FOV) region divided by number of pixels (matrix size). The spatial (through plane) resolution was slice thickness divided by number of slice frames. For high-resolution experiments, the matrix size was 1024×1024 and the volume of interest was 1500 mm³ to generate a pixel resolution of 15 μm and spatial resolution of up to 0.04 mm from 0.4 mm slice thickness containing a slice package of 10 slices. The voxel dimension for coronal and sagittal images was achieved at 1.0×0.4×0.04 mm³ (16×10^{−3} mm³) skin tissue voxel volume.

2.8. Image processing

The contrast enhancement between lipid-rich sebaceous gland and nonlipid hair body, epidermis and other dermis skin features was achieved by in vivo MRI parametric method to categorize skin structures based on their T2 values [26]. The denoising and surface-fitting segmentation were done by the ‘level set’ method to create a new volume from the input data to obtain a user-defined feature extraction as described elsewhere [26,27].

2.9. Quantitative assessment of skin structures

For rat skin images, the spin-echo signal intensity at different locations of skin structures was assessed as representative grayscale MRI signal of each skin structure in selected linear region of interest covering 4–16 pixels parallel to the surface (i.e., 0.6–2.6 mm in plane) and depth

Table 2

Different imaging protocols from Bruker Biospin PARAVISION 3.2 are shown with scan parameter settings and scanning times used to develop multiple contrast approach with the objective of discriminating different skin tissue structures in one or another imaging scheme

Contrast-weighted scheme	TR (ms)	TE (ms)	Scan time (min)
T1 weighted	100, 200, 500	8	6
T2* weighted	1000	16, 24	4
Proton density weighted	1500	10	5.5
Chemical shift weighted	50	10 and 45	6
MTC weighted ^a	7	700	10
DTI ^b	1000	33	12
GEFC	700 ms with flip angle of 20°	8, 8.3, 8.6, 8.9, 9.2, 9.5, 9.8, 10	0.3

^a Gradient-recalled-echo (GRE) pulse sequence MTC-weighted imaging of fat and water protons after saturation depends on the decreased magnitude of the water resonance as saturation is transferred from the fat to water. Four off-resonance saturation pulses were added for each phase-encode step. In addition, a spoiler gradient before each section-selection pulse diphases transverse magnetization as a result of the direct excitation of water by the off-resonance pulses. The 3D MTC sequence displays no ghosting artifact in the phase-encode dimension.

^b DTI-weighted 2D single-shot diffusion-weighted technique (2D ss-DWI) was used for time-efficient interleaved acquisition of multiple slices with a limited FOV by applying an even number of refocusing 180° pulses with the slice-selection gradient applied in the phase-encoding direction. The two refocusing pulses used for each slice acquisition were separated by a short time interval (typically <45 ms) required for acquisition. The large inhomogeneity in the static (*B*₀) magnetic field created by the magnetic susceptibility changed at the hair–skin dermis. The spins residing in the imaged slices were excited by the 90° RF pulse and subjected to a strong dephasing by the first diffusion encoding gradient. The first PE selective 180° RF pulse was applied to refocus the spins in the limited region of the imaged slice and at the same time inverts the spins in the out-of-slice region. After the second diffusion gradient signal readout, the second PE selective inversion/refocusing RF pulse was applied along *B*₀. The magnetization external to the imaged slice experiences two 180° pulses separated by a short time period (about 42 ms for an Echo Train Length (ETL) of 33) enabling interleaved multiple-slice acquisition. For calculation of DTI signal, a *b* value between 0 and 1000 was used to calculate *D* in DTI signal intensity $S = \text{intercept} \cdot e^{-bD}$ relationship.

of up to 2.5 mm. The MRI signal intensity and % MT activity profiles were assigned to anatomically identified skin layers (stratum corneum remnants, epidermis, papillary dermis and reticular dermis). For measurement accuracy, delineated areas on T2-weighted MR images were compared with delineated areas on coregistered histology digital images by the ImagePro software [27].

2.10. Optical microscopy

To compare and measure skin structures using histological data, the rat skin samples were processed in 10% formalin and immersed in fomblin and processed for histology of 4- μ m-thick sections using hematoxylin–eosin staining. In brief, 4- μ m-thick skin samples were dehydrated in a sequence of 70%, 90%, 100% ethanol and 20 s of hematoxylin staining followed by brief treatment of eosin and extra stain removal by xylene as described elsewhere [27]. Distinct skin layers of the epidermis, dermis, hair follicle, hair and sebaceous gland were assessed for skin viability and grade evaluation [27].

A quantitative MRI-histological index was developed for evaluation of skin grade and skin quality. The skin grade was I if hair root and hair body were intact and supported with unbroken hair follicle and sebaceous gland; grade II, if broken hair follicle; and grade III, if sebaceous gland is absent. The skin quality was based on the microscopic appearance of skin epidermis viable layers and viable vascular dermis layers. The skin quality was I if the epidermis layers of stratum granulosum, stratum spinosum and stratum germinativum were all visible by histology with distinct dermis layers of vascular reticular and papillary dermis; otherwise, poor quality II as described elsewhere [28].

2.11. Statistical methods

The histology–MRI correlation was done by using a nonlinear regression curve fit method using sensitivity–

specificity criteria, reproducibility test to avoid subjective bias and Student *t* test at two-tailed $P < 0.0001$ as level of significant match [27]. The sensitivity, specificity and prediction values were calculated by true-or-false, negative-or-positive (TP, TN, FP, FN) statistics of comparing skin hair and epithelium structures as described earlier [8].

3. Results

3.1. Microimaging probe and RF insert

The skin sample was tightly held in place enough between two 6.0-mm-wide Teflon plugs each time during imaging as shown in Fig. 1.

3.2. Phantom imaging

The water protons showed high signal intensity on proton density-weighted image. The mean value of T1-weighted signal intensity (in astronomical unit) \pm S.D. was 8.6 ± 0.2 in spin echo experiment, assuming the 55-M concentration was free from inhomogeneity. It served as water proton signal reference to compare the signal intensities of skin structures as shown in Fig. 2A and B. However, homogeneity was influenced by susceptibility, and the asymmetric bottle also contributed to the inhomogeneity.

3.2.1. Oil–water phantom

The signal intensity was measured in the region of oil and water interface in all the chemical shift images obtained. At 900 MHz, fat and water protons displayed the location of signal 3.5 ppm apart with a frequency difference of 3080 Hz. After every TE interval of 0.3 ms, in-phase and out-of-phase images were obtained. Gradient echo flow compensated images showed significant inhomogeneity effect as shown in Fig. 2C. However, oil-rich regions did not show distinct outer edges and uniform images due to inhomogeneity as

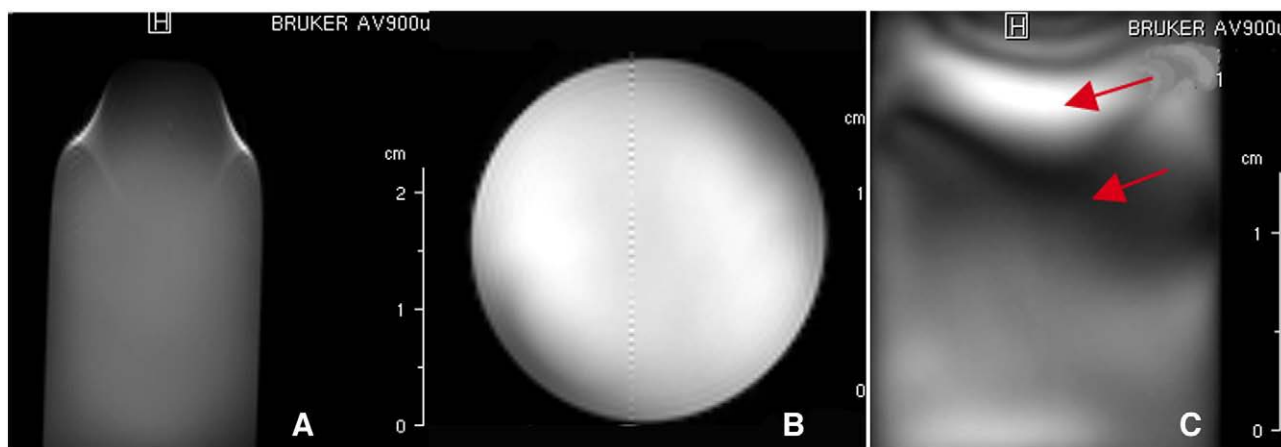


Fig. 2. The figure shows uniformity with least inhomogeneity on water phantom images (Panels A and B) by the multislice-multiecho (MSME) MRI method. The MSME technique showed least inhomogeneity on T1-weighted water phantom coronal image at TR=1000 ms and TE=10 ms (Panel A), and axial image (Panel B) at TR=1000 ms and TE=10 ms. The inhomogeneity effect was significantly visible on GEFC T2*-weighted image of oil (glycolipid) phantom (Panel C) at TE=10 ms and TR=700 ms. Notice the sensitivity of the T2* MRI signal with inhomogeneity due to fat–water phases shown as visible at the bottom of the phantom tube (see the arrow in Panel C).

shown in Fig. 3. However, the T_2^* -weighted signal intensities (see Fig. 3, Panels A–D in the right column) showed near to linear correlation with measured proton concentration (1–5 mM) in oil as shown in the histogram in Fig. 3.

3.2.2. Alginate bead phantom

Average T_2 -weighted signal of water between beads showed significant differences as shown in Fig. 4. The 50- μm -sized beads without free protons available appeared darker and measured $50 \pm 5 \mu\text{m}$ in diameter with a pixel resolution of $15 \times 15 \times 100 \mu\text{m}$ in a capillary of 0.5 mm internal diameter as shown in Fig. 4.

3.2.3. Teflon object

The proton density-weighted images by spin echo sequence showed distinct object dimensions without any blur as shown in Fig. 4.

3.3. Rat skin study

Average skin thickness was 0.6–0.8 mm on MR images. FLASH images generated a set of axial, sagittal and coronal images within 12 s. Coronal and sagittal skin images appeared similar due to the circular-shaped skin samples.

These images were used as guides for placing volumes of interest box for 2D and 3D multislice long scan experiments. The skin epidermis thickness ranged from 150 to 200 μm .

3.4. Multiple contrast image characteristics

The combined approach of different MR modalities shown in Table 2 showed distinct skin structures at different weighting schemes as shown in Table 3 and Fig. 5A–E. The outermost stratum corneum was brightest on T_1 -weighted images as shown in Fig. 5A. The epidermis was brightest on T_2^* images as shown in Fig. 5B. The dermis appeared brighter on both T_1 -weighted and proton density-weighted images. The hair follicle was brighter on DTI and T_2^* -weighted images as shown in Figs. 5C–D and 7B. The sebaceous gland was distinct and brighter on MT images as shown in Fig. 5D.

3.5. T_1 - and T_2 -weighted imaging

Each skin component showed distinct T_1 relaxation constant. The outermost remnants of the ‘fuzzy layer’ at the surface of the rat skin indicated the thickened stratum corneum, which represented bright signal intensities as shown by the arrow in Fig. 5A. T_1 -weighted images at

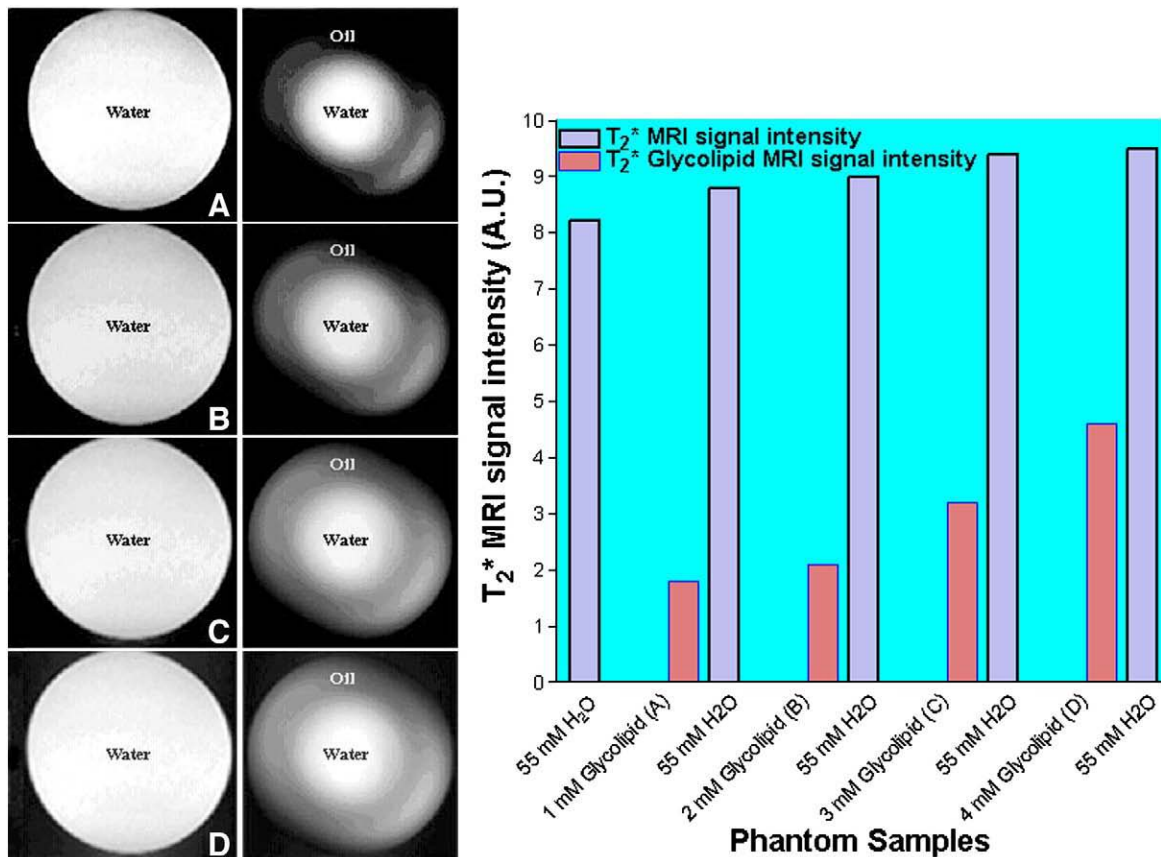


Fig. 3. (Left) The water T_1 -weighted high signal is shown in the first column. The multislice-multiecho T_1 -weighted spin echo sequence was used at $TE=10$ ms, $TR=1000$ ms, $NEX=2$. The T_2^* signal intensities of oil–water phantom (A–D) at 1–4 mM glycolipid concentration in the outer tube and high water T_1 -weighted signal in the inner tube are shown in the second column. (Right) GEFC T_2^* -weighted signal intensity of oil (glycolipid) is compared with water signal intensity in oil–water phantom tubes (A–D) as shown by histogram bars.

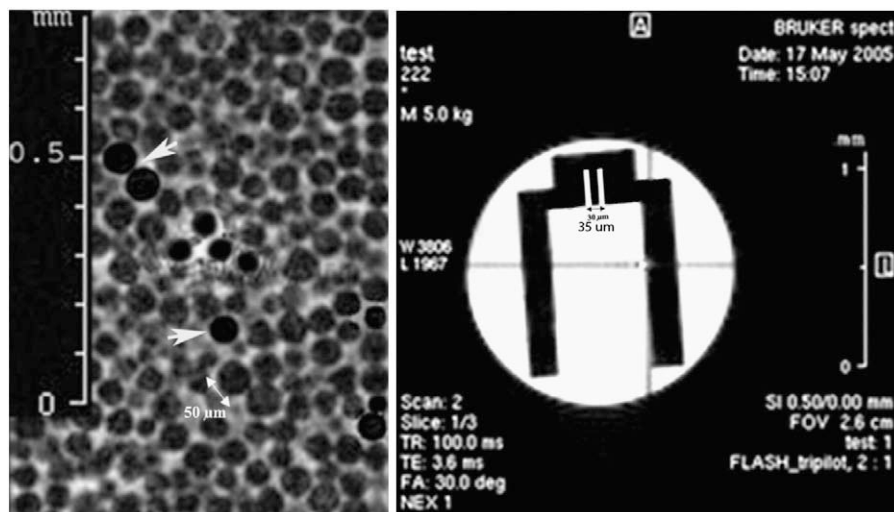


Fig. 4. The figure represents the measurement accuracy of a high-resolution image of 50- μ m-sized alginate beads shown with arrow (on left panel) and the possibility of measurement on high-resolution axial image of a 1-mm Teflon plastic object inside a tube (on right panel). Notice the measurement limit of up to 15 μ m shown with arrows on the image. The proton density images were acquired with triplot spin echo sequence used at TE=3.6 ms, TR=100 ms, NEX=1. Notice the structural details of the Teflon object on the image in a total scan time of 12 s.

TE=8 ms and TR=100–700 ms showed distinct T1 relaxation time constant values (mean \pm S.D.) for skin layers at different locations as: (T1)_{stratum corneum}=60 \pm 5 ms, (T1)_{epidermis}=375 \pm 12 ms, (T1)_{papillary dermis}=375 \pm 17 ms and (T1)_{reticular dermis}=269 \pm 16 ms. In Fig. 5A, the skin T1-weighted image is shown at TR=500 ms. It indicates the nature of the epidermis rich in free water content. In a T1-weighted image at short TR=100 ms, the skin epithelial contrast (SEC %) was 18%, which is less than the T2-weighted image at a long TR=2000 ms. A T2*-weighted image of the rat skin at short TE=8 ms showed the outermost remnant fuzzy layer of the stratum corneum and long TE=20 ms showed distinct sebaceous oil gland (Fig. 5B). It indicates that the stratum corneum remnant had a short T2 perhaps due to its glycolipid-rich content made of dry and dead cells.

3.6. Fat-water chemical shift imaging

The fat-water contrast shown in Fig. 5C indicates the presence of the fat and water composite signal. In Fig. 6A, in-phase (water plus fat) skin water images showed sharper

morphological features of the dermis and hypodermis layers at TE=10 ms. However, at TE=8.3 ms out-of-phase (water minus fat) skin fat images showed better contrast (Fig. 6B). The dermis layers of fatty acid-rich reticular dermis differed from papillary dermis and showed signal loss compared with the papillary dermis. The ‘chemical shift difference effect’ created morphological contrast between the dermis and hypodermis based on phase shift difference between fat and water. The hypodermis layer was made of mainly fat-rich adipose tissue consisting of fat cells invaginated within the fibrous tissue in the reticular dermis. Out-of-phase signal from ‘water minus fat’ phase images shown in Fig. 6B provided the possibility to distinguish localized fat cells from fibrous lattice. However, edge detection with distinct boundaries was difficult.

The fat-water chemical shift image contrast in the regions of reticular and papillary dermis tissues was comparable with oil–water phantom as shown in Fig. 6. The water-phase MR images showed better skin morphology, while fat-phase images showed distinct fat-rich regions of the skin. Both these images and water-fat characteristics were echo delay

Table 3

Different skin appendages and their relative MRI signal intensities at different scan parameters

Skin appendage (1)	T1-weighting (2)	T2*-weighting (3)	Proton density-weighting (4)	Magnetization transfer-weighted (5)	Diffusion tensor weighted (6)
Stratum corneum	Brightest; ++++	Darker-gray	Isointense	Brighter; +++++	Dark
Epidermis — stratum spinosum	Isointense	Brighter; +++	Brighter; ++	Isointense	Dark
Dermis — Reticulum	Brighter; +++	Gray	Brighter; +	Gray	Brighter; ++
Dermis — Papillary	Bright-Gray; ++	Dark gray	Brighter; +	Dark gray	Isointense
Hair follicle	Gray	Brighter; ++	Dark	Brighter; +	Brighter; +++
Sebaceous gland	Isointense; +	Hyperintense; +	Brighter; ++	Brighter; +++++	Brighter; +

Different MRI signal intensity grades are shown to distinguish different skin features (in Column 1) as ‘+’ for brighter signal with various grades, isointense for no change, gray for moderate decreased signal and dark for no signal. Multicontrast MRI features are shown for each of the imaging techniques (in Columns 2–6) for relative signal intensity as shown in Fig. 5.

time (TE) dependent. The image contrast demonstrated the in-phase and out-of-phase interplay of the fat and water-sensitive MRI signals at two different TE settings applied on the T2* decay. The fat-rich reticular dermis signal intensity showed distinct in-phase and out-of-phase interplay similar to the water–oil phantom chemical shift contrast but distinct from fat-free papillary dermis as shown in Fig. 6A and B.

3.7. MTC Imaging

The MT pulse sequence using GE technique with MT pulse (TE=8 ms, TR=700 ms) generated control and MT

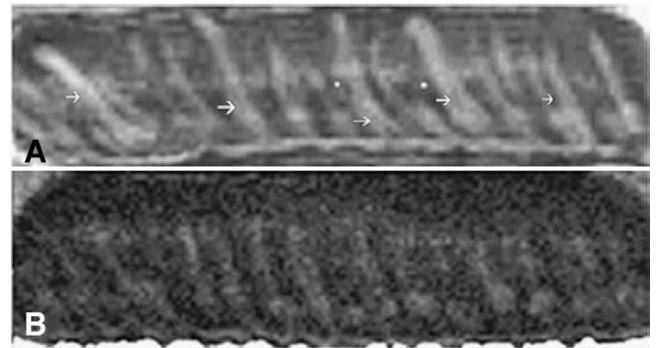
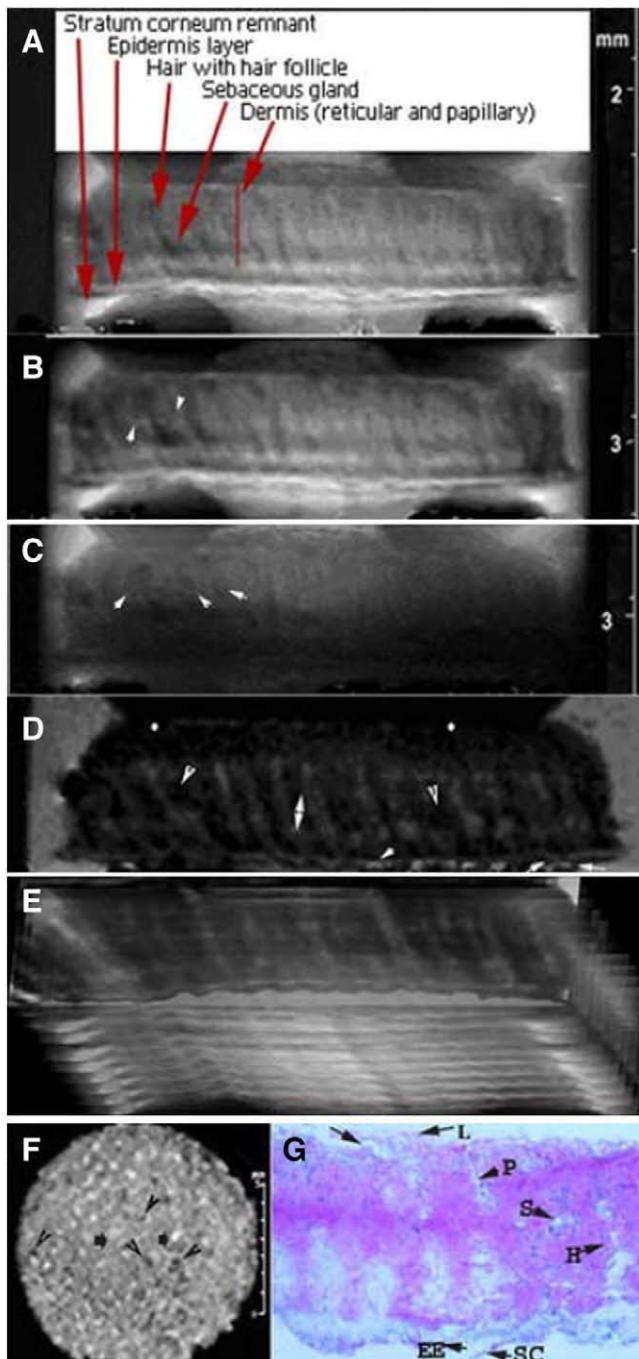


Fig. 6. The fat-water chemical shift images are shown as a proton density-weighted image (water phase only) at TE=10 ms (A) and TE=8.3 ms (B) (fat phase only) by the T2* GEFC imaging method. The image signal intensity with the in-phase echo time (TE=10 ms) for the interface between the dermis and hypodermis (in A) was higher than the out-of-phase echo time (TE=8.3 ms) (in B). The hair follicle rich in water (arrow in A) and oil-rich sebaceous glands (white dot in A and brighter in B) show the fat-water phase contrast. However, the overall signal intensity in (B) was degraded due to longer TE and less scan time.

images and represented the magnetizations M_s and M_0 distribution as shown in Fig. 5C. The M_s magnetization distribution represented tissue proton relaxation and magnitude of transfer. From these two images, mean±S.D. of the percentage MT activity $[(1-M_s/M_0)-100]$ was 85 ± 13 . The images were reproducible for MT measurements. The low MRI signal intensity of the stratum corneum remnants showed poor external skin layer. The GEFC signal intensity of the epidermis showed an increased and elevated skin epidermis contrast (SEC) of 27%.

3.8. DTI Imaging

The DTI standard (Bruker Biospin, CA) protocol generated grayscale MR images from reduced diffusion-weighted dataset with distinct diffusion tensor intensities of encoded information about the spatial orientation of collagen fibrous makeup in the skin. The distinct skin hair diffusion anisotropy distribution at two spatial locations in principal diffusion

Fig. 5. Different rat skin MR images are shown using multicontrast method for coronal skin images. Different skin structures are shown distinct on coronal T1-weighted (A), T2-weighted (B), MTC-weighted (C) and chemical shift-weighted (D) images with arrows. Notice the visibility of different skin structures on different weighting images based on fat (white dot in D), epidermis (in A and D) and hair within hair follicle (B and D). Each skin structure is visible on one or more weighting images. A 3D MSME proton density-weighted skin slab is shown with different skin planes (E). Notice the dimensional clarity of the skin structures on 3D slab. For clarity of hair (arrowheads) and glycolipids (arrows) on skin surface, a T2* axial image (F) is shown. The MRI scan parameter setting is shown in Table 2 at different TE and TR values for each technique. Matched histology 5- μ m digital image is shown for skin structure details of the epidermis (EE), stratum corneum remnant (SC), hair (H), sebaceous gland (S), papillary dermis (P) and hypodermis lipid (L). The MRI scan parameter setting is shown in Table 2 at different TE and TR values for each technique. Notice the distinct dark lipid-rich sebaceous gland with arrowheads and water-rich hair follicle regions with arrows in chemical shift images (D).

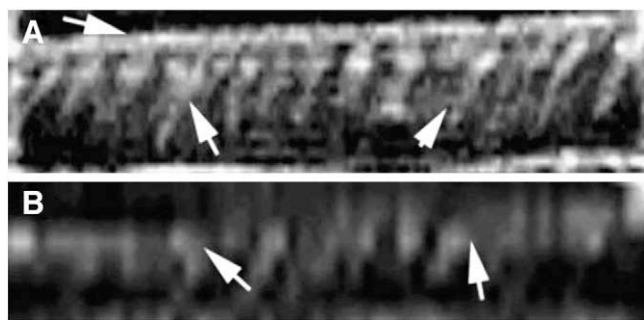


Fig. 7. A representative skin DTI-weighted image shows a spatial anisotropy map of water molecule diffusion (tensor map) in hair, hair follicle, dermis and hypodermis (arrows, Panel A) and anisotropy map of fat diffusion tensor map in sebaceous gland (arrows, Panel B). Notice the hair and epidermis appear different in two images with distinct hypodermis and sebaceous gland due to different anisotropy of the protons. The parameters were set as TR=5000 ms, TE=18 ms, NEX=1, matrix=128×128, FOV=0.1×0.8 cm.

directions is shown in Fig. 7A in one spatial orientation and Fig. 7B in another spatial orientation with diffusion tensor contrast. The hypodermis layer was distinct on DTI image. However, edge detection and distinct boundaries were poor at the cost of longer scan times of up to 20 min.

3.9. Resolution

The ultrahigh pixel resolution was achieved up to the level of 15 μm and spatial resolution of 40 μm of 10 slice packages from 0.4-mm-thick slice thickness at a FOV of 1500 mm³ and matrix size of 1024×1024. The spatial resolution was based on the selection of 10 slice packages to achieve 3D slab. However, more than five times out of twenty 3D imaging experiments using high-resolution 3D protocol prescription interrupted the experiments in the middle with the result of overuse of RF coil and fast switching gradients for longer time. We minimized the chance of interruption by selecting optimized slice thickness, volume of interest and matrix size as mentioned above. These conditions restricted further fine pixel resolution of up to 15 μm . The spatial resolution maximum limit was 0.04 mm achievable by selection of 0.4 mm slice thickness using multislice-multiecho spin echo technique to generate high-resolution images at the cost of longer scan times of up to 45 min.

3.10. MRI Signal inhomogeneity and noise characteristics

The use of ultrahigh magnetic field of 21 T with strong gradients generated inhomogeneity and higher noise (Fig. 8A) on high-resolution GEFC images, although it produced better fat-water contrast. The denoised or less grainy images after convolution in k -space showed the SNR enhancement (Fig. 8B), and inhomogeneity correction by gradient-based approach showed clear skin structures (Fig. 8C).

3.11. Image processing

The contrast enhancement between lipid and nonlipid skin structures using ex vivo MRI parametric segmentation

method categorized the skin structures based on their different T1, T2, MTC and DTI image signal intensities as shown in Fig. 9. The line histogram bars represented different skin structures as shown in Fig. 9 with different arrows in the panel at the bottom.

3.12. Parametric imaging and segmentation of skin features

The denoising and surface-fitting segmentation by the 'level set' method are shown in Fig. 9 (top row). The method created a new volume from the input data by using an initial value partial differential equation with user-defined feature extraction as shown in Fig. 9 (rightmost panel).

3.13. Optical microscopy and histology–MRI correlation

Fig. 10 shows a histological digital image of the rat skin sample, and the corresponding MR image as shown in Fig. 9B. On average, histological digital images showed 10–15% lower skin measurements compared with MRI skin measurements. Comparing the MRI and histological images in Fig. 10A and B, the viable epidermis of the rat skin was a distinct 200- μm cellular skin layer comparable with the approximately 0.2 mm or 4 pixels of bright band in the MR image (Fig. 10B). This demonstrated a match and measurement accuracy between MRI and histological data as shown in Fig. 10. These skin MRI visible features of the epidermis, dermis,

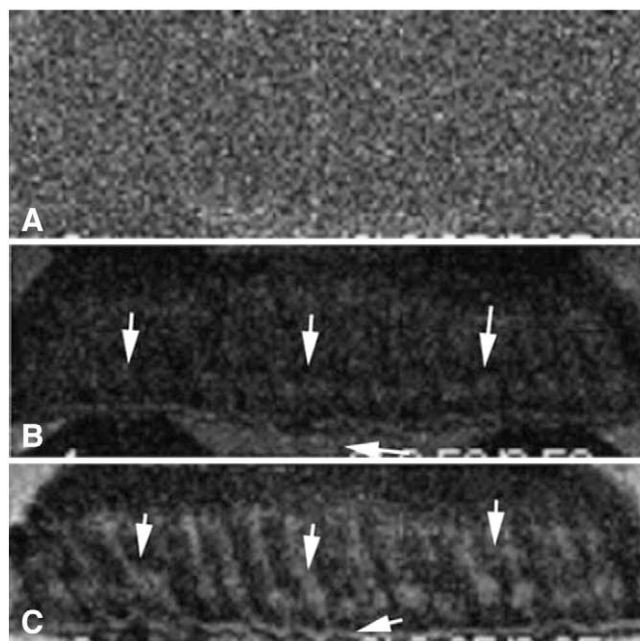


Fig. 8. The figure represents the inhomogeneity correction by gradient-based correction method for T2*-weighted GEFC images. Panel A is a noisy image without correction. The image in Panel B was obtained with partial inhomogeneity gradient-based correction and that in Panel C was obtained after full inhomogeneity gradient-based correction with suppressed noise by convolution in the k -space. Notice the contrast of skin epidermis, hair and hair follicle structures shown by arrows was sensitive to inhomogeneity correction method in Panel C.

hair body and sebaceous gland were distinct after segmentation as measurable shapes to compare with skin histology morphometrics. The skin quality in seven samples was Grade I (two of seven skin samples), Grade II (three of seven skin samples) and Grade III (one of seven skin samples). However, the skin features of different grades were not visible in all samples. The skin features visible in the samples out of total samples with different grades are shown in parentheses above. However, the skin epidermis was deformed after long scan hours of the skin in phosphate buffer saline and overestimated the skin epidermis on MR images.

3.14. Sensitivity and specificity of histology–MRI correlation

The rat skin hair follicle and epidermis areas delineated on representative T_2 MR images and matched with histology digital images showed a sensitivity of 77.7%, specificity of 11.1%, accuracy of 83.3% and precision of

66.6% ($n=9$ skin images) for comparisons. For comparisons, true positives=7, true negatives=3, false positives=1, false negatives=1, total observations=9 and incomplete observations=3.

Individual skin structures were further measured on MR images and histological images to evaluate the compositional and dimensional details of each layer.

3.14.1. Epidermis

The epidermis layer demonstrated high GEFC signal intensity and a 27% SEC higher percentage MT activity over other skin layers. The epidermis was a 200- μm -thick layer made of distinct layers. These layers were visible by histology as stratum granulosum, stratum spinosum and stratum germinativum layers as shown in Fig. 10A.

3.14.2. Dermis

The dermis measured 750–800 μm thick. The dermis was rich in collagen fibers and bound water-rich semi-fluid

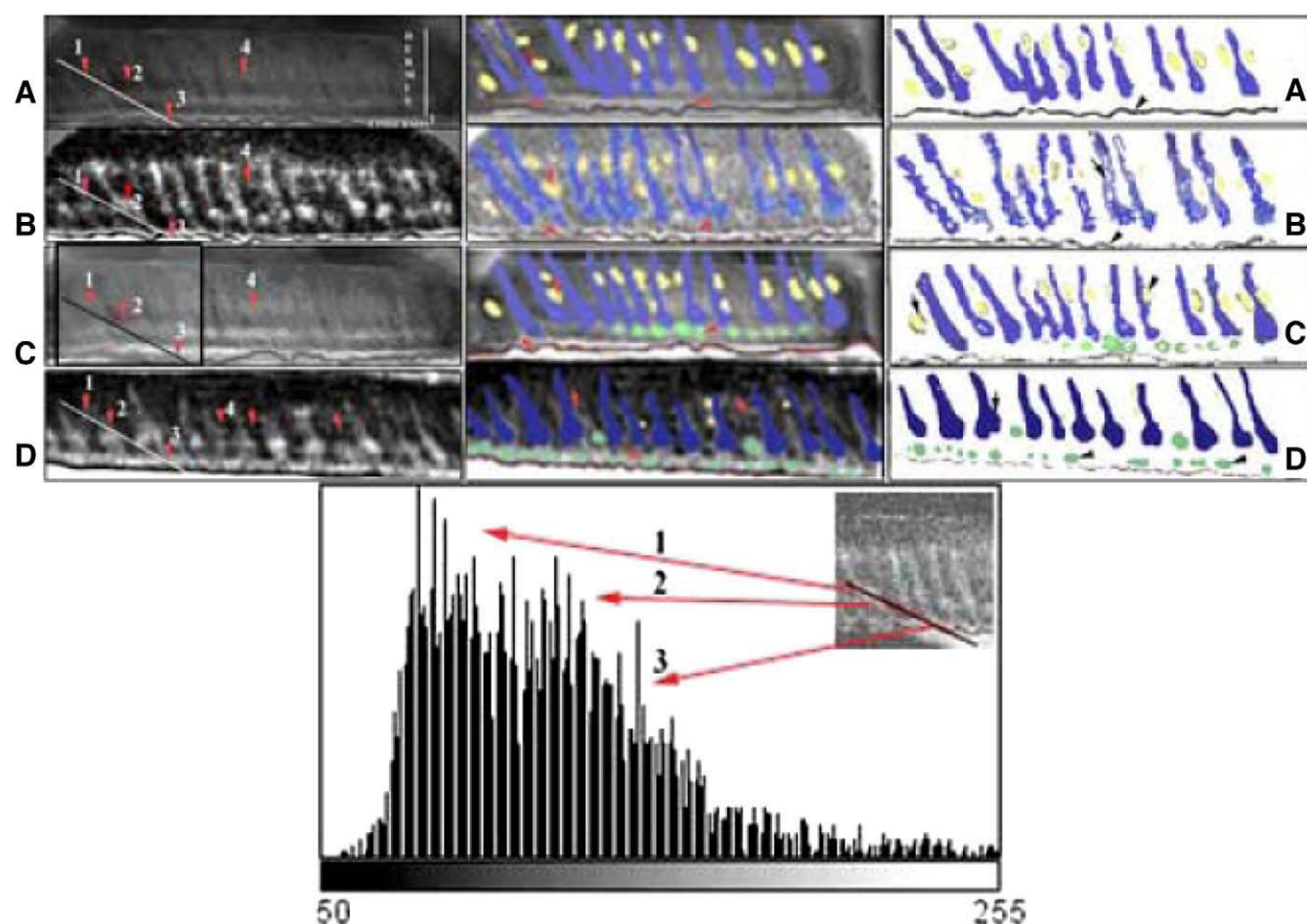


Fig. 9. For comparison, coregistered images of rat skin are shown as coronal slice using multiple contrast techniques. From top, T1-weighted (A), T2-weighted (B), MTC-weighted (C) and reduced DTI-weighted set (D) are shown as row (Panel A), color-coded segmented skin structures (Panel B), extracted-out skin structures (Panel C) with arrows for sebaceous gland (1), hair follicle (2), epidermis (3) and hypodermis fat (4). Notice the selective MRI visible skin structures on different contrast weighting (A–D). Post segmented by threshold trained data set and color-coded coregistered rat skin images are shown after ‘level set’ feature extraction without background skin tissue. Notice the distinct hair body (blue) with sebaceous glands (yellow) and epidermis (dark red) and hypodermis lipid (green). Line histogram features are shown for each skin structure with arrows for sebaceous gland (1), hair follicle (2) and epidermis (3) matched with MR image (on Panel A).

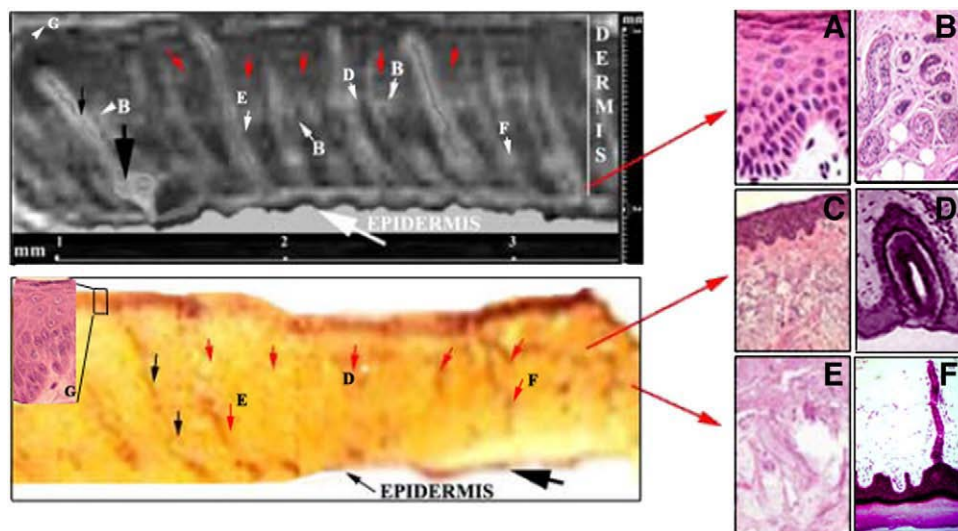


Fig. 10. A representative skin T2-weighted MR image is shown (left panel on top) and matched masked histology section of skin (left panel at bottom) for comparison. The skin histology features by high power microscopy ($\times 400$) show the epidermis layer (A) made of stratum granulosum (SG), stratum germinativum (SGr), stratum spongiosum (SS) and stratum basale (SB); sebaceous gland (Sb) (B); reticular dermis (RD) and papillary dermis (PD) (C); hair follicle (D); oil gland (E); sweat gland (F); and hypodermis (G) with other vascular features of the dermis layer (see panels on right). Notice the resolution of MRI microimaging on scale to distinguish hair and its hair epithelium wrapped around it up to 70 μm .

vascular tissue. It showed lower 18% MT activity compared with the epidermis. Both papillary dermis and reticular dermis layers of the dermis showed distinct histology and cellular characteristics as shown in Fig. 10B and 10C (inserts). Both layers showed different MT contrasts and MRI signal intensities with the following tissue characteristics: (a) The papillary dermis was thin and closely packed with collagen fibers due to interaction between collagen (i.e., bound water) and free water, which is the reason for the higher % MT activity compared with the reticular dermis. (b) The papillary dermis showed fibroblasts and other specialized Merkel cells showing more cellular characteristics than the reticular dermis. (c) The reticular dermis showed fatty inclusions from the adipose tissue-rich hypodermis.

3.15. Hair follicle and sebaceous gland

The hair body measured up to 500 μm with 80- to 100- μm -thick hair root and 100- to 150- μm -thick sebaceous glands on T2-weighted images as shown in Figs. 10 and 11. However, histological digital images showed lower measured dimensions due to histological tissue processing. For example, hair follicle areas (mm^2) measured by histology were 15–20% smaller than areas measured by MRI because of shrinkage of skin tissue during histological tissue processing (correlation coefficient $r^2=0.4927$ for MRI area, and $r^2=0.3068$ for histology area; $P<0.0148$) as shown in Fig. 12 and Table 4. It indicated that the calculated values of area by MRI and histological digital images did not agree as shown by the low P value due to the well-known fact of tissue shrinkage due to tissue histological processing.

4. Discussion

In the present study, rat skin tissues were used because the rat skin is appropriately 0.8–0.9 mm thick, which is easily available for visualization of skin layers and interpretation of the skin structures. The RF insert microimaging probe (10 mm internal diameter) was used to house the skin sample in a 900-MHz (21 T) microimager to achieve high signal strength from the region of interest in magnet at its center. Other ex vivo studies also suggested the benefit of fractional imaging at the center of k -space to reduce data acquisition time [8]. The major findings were as follows: (1) fat-water MRI contrast, measurement accuracy and ultrahigh resolution were improved by using the 900-MHz MRI microimager; (2) the multiple contrast using T1, T2, T2*, PD, MTC and DTI techniques visualized almost every skin structure; (3) the denoising and inhomogeneity minimization reduced the inhomogeneity and noise due to the use of a 900-MHz microimager on GE images; (4) multislice-multiecho SE images generated high-resolution images; (5) the skin hair and epidermis structures on MRI were comparable and measurable by histology. The present study highlights the high MRI signal with high spatial resolution and contrast of MRI visible skin structures is of scientific value in 900-MHz MR microimaging experiment.

The water protons in the phantom tube generated high proton density signal by 900-MHz MR microimaging. The oil–water phantom served as a model of ‘water minus fat’ contrast depending on their frequencies at selected TE parameter. This fat-water contrast created brighter signals for water and lower signals for fat as shown in Fig. 2 which corroborated with other reports [22,23]. In a separate study, a

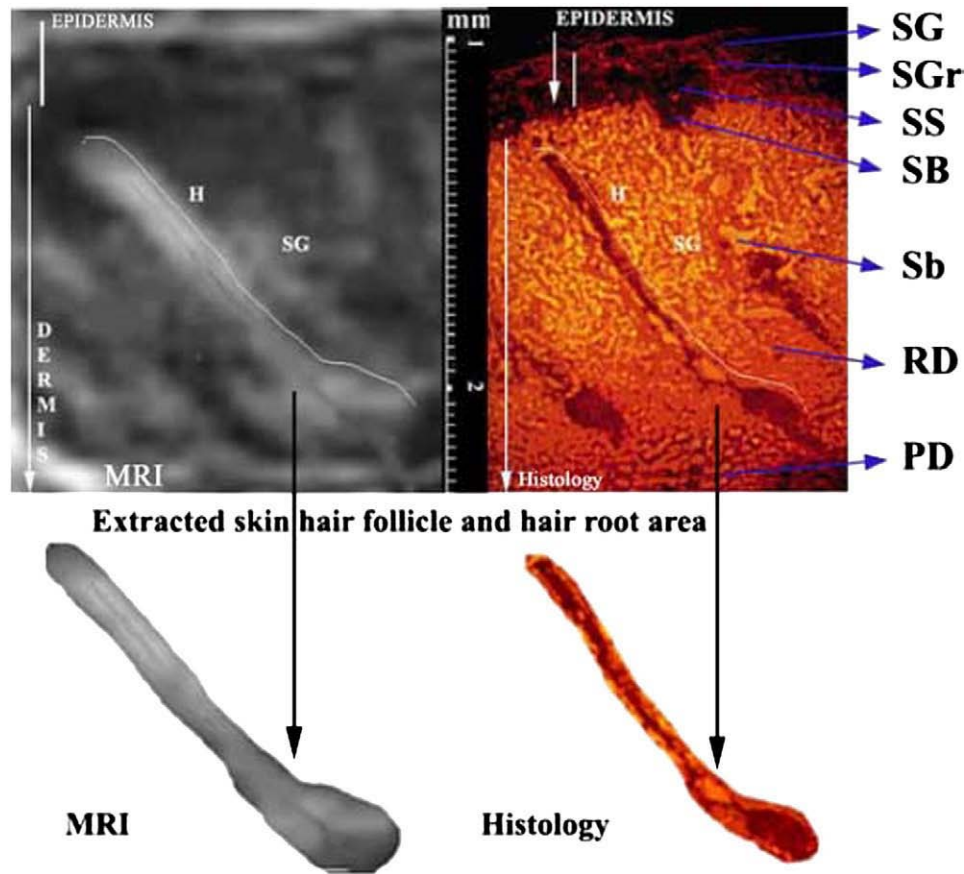


Fig. 11. The figure represents the match between a MR image and coregistered histology digital image (panels at the top). The segmentation automated tracing method of delineation of the extracted area is shown on both images. The scale on the image highlights the high-resolution measurement of skin features up to a level of 20 μm . The histology visible skin features are shown with arrows and abbreviated as shown in Fig. 10.

comparison of these images with theoretical predictions was performed to obtain images based on the point spread function model (not shown here). The selective adjustment of RF pulses and spoiler gradient pulses to dephase transverse magnetization produced the ability to distinguish the water protons from fat protons. It generated fat-water images at different TE values with in-phase and out-of-phase effects as distinctly separate oil and water images. The concentration of oil fat in phantom tubes showed linear correlation with SNR was achieved after utilizing enough coil filling factor during the image acquisition. The increased fat protons in the phantom showed increasing SNR due to the dependence of oil-induced T_2^* shortening effect on oil proton population in the sample, and other reports also suggested a similar relationship should be applied when measuring skin fat in vivo [23,24].

The phantom of oil containing glycolipids showed distinct MRI properties of water protons due to phase shift of fat-water protons on MR images. However, the large phase shift was dependent on the strength of applied 900-MHz magnetic field. The similar fact of lipid phase shift was demonstrated recently to develop the quantification approach applied to distinguish tissues [9,23]. The alginate beads demonstrated the measurable limit of up to 20 μm at

900-MHz high resolution. Another unique feature of 900-MHz microimaging was dimensional accuracy as demonstrated by a 1-mm plastic object image.

In our experiments, magnetization of individual slices was excited by selective 90° RF pulses and refocused by selective 180° RF pulses to get more than one echo using $TE=10$ ms. However, other report showed that a fast repetition caused saturation but provided high T1 contrast [10].

At 900 MHz, high-resolution rat skin MR images on multiple contrast display showed distinct image contrast characteristics. Different skin structures of the stratum corneum, epidermis, papillary dermis, reticular dermis and hypodermis appeared with distinct molecular nature. The study presents for the first time the 900-MHz MR microimaging capability of rat skin imaging using multislice, MTC, DTI techniques to generate multiple contrast with dimensional and compositional properties of skin structures. A similar multiple contrast approach may serve as a guideline to other high-resolution, ultrahigh contrast imaging studies.

4.1. T_1 -weighted imaging

Longer repetition times (TR) generated higher signal level at the cost of lengthy imaging scan time. So, the choice of short TR was to complete multislice-multiecho experiments

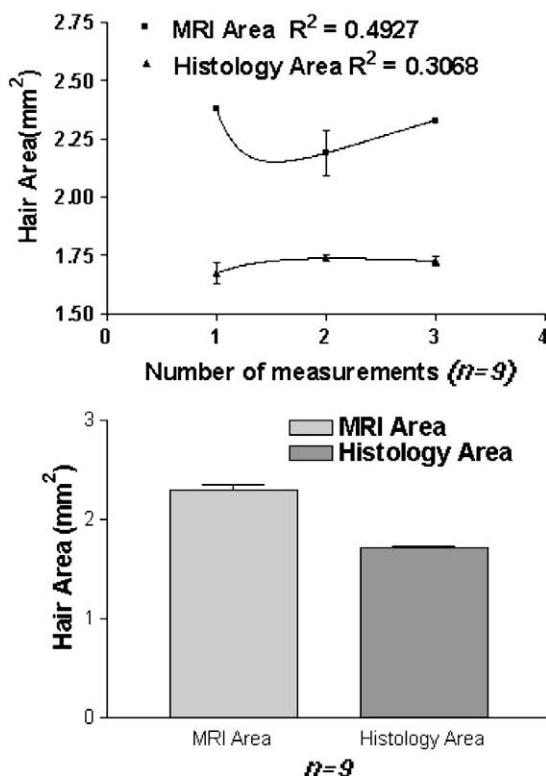


Fig. 12. The graph represents the comparison of the area measured by MR image and coregistered histology digital image ($n=9$) with correlation analysis (top panel). The comparison is shown (mean \pm S.D.; $n=9$) as bars for area measured by MR image and coregistered histology digital image (bottom panel).

within 2–3 minutes. Different skin tissues display a wide range of T1 relaxation constants for long T1 species as darker and short T1 species as brighter. So, different selected TR values may determine the contrast enhancement between the skin tissues of interest. Contrast due to T1 relaxation constant differences of semi-fluid skin structures (T1-weighting) was better at short TR with a distinct visible effect on signal intensity. In our experiments, a minimum TE=8 ms was used with a wide range of shorter TR between 300 and 500 ms to achieve high contrast with T1-weighted display of distinct skin structures.

4.2. T2*-weighting imaging

At longer TE times, soft skin tissues displayed better T2* contrast between tissues using a longer TR set increased up to 2000 ms. The T2*-weighted images showed long-T2* species appearing brighter than tissues with shorter T2*.

4.3. Fat-water contrast

The water protons in skin tissue can be represented as two pools of proton spins. The first pool consists of protons associated with 'free' water molecules, which are mobile and MRI detectable (corresponding to a long T2). The second pool consists of protons in 'bound' water molecules, which have restricted movement due to their binding with

macromolecules [23]. These bound water protons have shorter T2 and are MRI invisible. Water proton precession differs in frequency shift by 3080 Hz relative to fat protons in the 21-T system used in this study. This difference generated MRI contrast of fat and water signals originating from the same tissue volume. It may define the lipid–water phase difference of MRI signals from two types of water or lipid protons after every 0.3 ms, i.e., in-phase at TE=9 ms and out-of-phase at TE=8.7 ms. The MRI contrast based on interplay of proton pools further visualized the microscopic chemical environments inside the rat skin. Oil–water phantom distinguished clearly the oil-rich regions of the sebaceous gland and the mobile lipids in dermis accessible to mobile water protons.

4.4. Magnetization transfer contrast

The MTC contrast techniques of fat-water contrast appear to investigate skin properties in a noninvasive ex vivo manner. The MTC-MR contrast technique detected the outer edge of the stratum corneum remnant and other motion-free constituents of skin layers. The MTC contrast was more sensitive to the protons associated with water or fat. Furthermore, the saturation pulses applied in the MTC technique may saturate the MRI signals from the bound water protons. Thus MT pulse enables the 'magnetization transfer' from free-to-bound protons and reduces the other tissue signal intensities [5,7,16–20,29,30]. The signal attenuation in skin tissue enhanced the contrast or magnetization transfer ratio (% MT activity). So, the water pool would attain contrast if the bound pool were held in a state of saturation indefinitely [5]. The ratio of M_s/M_0 depends on the saturation RF pulse amplitude. In the present study, the interleaved acquisition of skin tissue images was free from motion artifacts and misregistration between measurements at TR=700 ms. It leaves a time delay between MT data acquisition and excitation for the control-GE image. Previous reports suggested that this scheme allowed for relaxation of both bound and free water pools prior to the next excitation [8]. The present study also corroborated with the fact that the

Table 4

Comparison of MRI area vs. histology delineated area measurements

Area measured ($n=9$)	MRI Area (mm ²)	Histology area (mm ²)
1	2.3655	1.5835
2	2.3750	1.7377
3	2.4025	1.7000
4	2.0155	1.7255
5	2.2350	1.7225
6	2.3355	1.7655
7	2.3434	1.6976
8	2.3253	1.7217
9	2.3215	1.7623
Mean \pm S.D.	2.302 \pm 0.0959	1.713 \pm 0.0343
Standard error	0.0554	0.01983

The paired t value=8.136; $P=0.0148$; correlation coefficient (r)=0.4369 using nonlinear regression analysis. The runs test showed linear relationship.

MTC technique offers the possibility to visualize short T2* skin structures using short echo time to achieve short echo T2* images. However, this pulse technique has an unavoidable drawback due to its sensitivity to longer T2 species. In the present study, we used optimum pulse amplitude to achieve the best MT contrast with less than 10% effect on the skin free water.

The MTC technique visualized the epidermis and distinguished it from the stratum corneum remnants on MTC images. These images may have the potential to monitor the thickness of the outer skin after treatment of skin diseases. However, nude rat skin showed the outer edge of the stratum corneum remnants by MTC. The collagen-rich dermis with bound water-rich semi-fluid tissue and low free water content perhaps was the reason for the lower percentage MT activity observed in the dermis compared with the epidermis. The distinct layers of papillary and reticular dermis layers as MRI visible skin features suggested that the MT activity is sensitive to lipid-rich feature distinct from the vascular features. It could be the reason for the lower MT activity in the reticular dermis and high MR signal intensity of the papillary dermis. Our results corroborate with earlier reports on in vivo skin features by high-resolution MRI [9,11,31].

4.5. Diffusion tensor imaging

For DTI, the skin tissues were assumed as nonspherical geometry on water diffusion boundaries leading to diffusion anisotropy. DTI technique mapped the anisotropy of hair follicle and collagen dermis fibers at each spatial location. Other study used tensor formalism as tensor elements with other quantitative possibilities of scalar diffusion anisotropy indices, diffusion coefficients, apparent diffusion coefficients, traces, tractography and vector maps suggested DTI as a quantitative MRI tool [32].

4.6. MRI–histology comparison

The hair features, epidermis and dermis skin layers showed averaged MRI signal intensities within seven control samples. The ex vivo MR images could be calibrated by co-registered histology of excised rat skin tissue. The measurement represented the dimensional comparison of ex vivo MR images with skin structures on histology sections. The skin hair body area measurement was most convenient to compare area on both MRI and histology images. However, skin histology measured 10% less due to shrinkage of skin tissue during histology tissue processing. The quantitative comparison of hair follicle areas indicated low *P* values and different histological-MRI measurements. It further suggested MR images as truly representative of skin structure dimensions at physiological conditions.

The T1 relaxation constant values as T1 signal intensities were measured shorter (approximately 40%) in this study compared with the values published in a previous work [33]. The reason for the short T1 measures is that short TE was not

applied in the present study. However, total imaging time was reduced by a factor of 10 to achieve steady-state condition. The total imaging time in the previous study was 60 min using TR=4000 ms [10].

All rat skin samples showed distinct skin epidermis contrast (% SEC). In all images of different rat skin samples, the epidermis appeared as a dark band with the highest signal intensity beneath the surface gray layer of the stratum corneum remnants, and also a higher T1 value compared with the stratum corneum. These results may be due to the higher concentration of water in the epidermis compared with the stratum corneum. This is consistent with the morphology of the epidermis having a high cellular component made of different viable layers of the stratum granulosum, stratum spinosum and stratum basale, which gives rise to an interstitial space filled with extracellular fluid as shown in Fig. 9. Other studies support our observation of improved correlation of histology data with MRI data by the parametric approach [9,28].

4.7. Advantages

The use of high magnetic field gradients increased the high spatial resolution in MR images. Also, SNR was affected by the field gradients indirectly due to short data acquisition times. Strong gradients proportionately enhanced the inhomogeneity and thermal noise due to B_0 in fat-water phases during microimaging as shown in Fig. 8. However, homogeneity was not measured but thermal noise was independent of magnetic field. The pixel resolution of up to 15 μm and 0.4 mm spatial resolution were advantages of MR microimaging for T1, T2* and proton density-weighted images. Different skin structures of the stratum corneum, epidermis, papillary dermis, reticular dermis and hypodermis appeared distinct on different weighting schemes. It remains to be seen whether advanced image postprocessing can combine all images at different weighting schemes to generate a composite image showing the detail of each skin structure and distinct layers with their specific MRI signal intensity values. Each skin MR image of 0.5 mm slice is represented as a composite of 100 histology images from 5- μm -thick histology sections. The present study was limited to fresh excised skin tissue microimaging and has potentials to study live skin samples from experimental disease models, pharmacotoxicity and allergen-induced effects. The study has tremendous value as a noninvasive imaging method in both experimental and clinical MRI in dermatology, cancer and cosmetics.

4.8. Limitations and disadvantages

During imaging, the skin rested on the imaging platform and the outer edge of the epidermis layer touched a flat Teflon plate to obtain micrometer-level details of each epidermis sublayer. The presence of air bubble at the interface between the Teflon plate and epidermis may cause a susceptibility artifact and misinterpretation of the real

thickness of the epidermis layer if Teflon plates are not tightly placed in the NMR tube. The ultrahigh-resolution MRI suffers from various physical effects such as Faraday shielded vs. temperature rise, susceptibility, signal variation due to RF coil or B_0 over field-of-view region, dielectric resonance phenomenon, RF penetration and induced heating as common interfering factors to generate noise-free images. Another disadvantage of using high magnetic field gradients was the reported high tissue specific absorptive ratio during in vivo imaging experiments using short TR [12]. The quantitative MRI–histology correlation is based on measurements but still qualitative since it was totally dependent on subjective assessment.

Our results are the first preliminary report on normal rat skin MR microimaging at 21 T to investigate the possibility of multicontrast features of the epidermis, hair follicle, dermis, remnants of stratum corneum and hypodermis extracted out from 2D multislice and 3D slab skin image frames. The study highlighted the possibility of fat-water protons and optimized scan parameter settings of TE and TR as tools to generate additional contrast to distinguish skin features. These skin features may considerably vary when pathology alters the water concentration, cross-relaxation, macromolecular composition of the tissue or macromolecular dynamics.

5. Conclusions

High magnetic field 900-MHz MR microimaging may generate ultrahigh resolution with water-fat contrast by multicontrast imaging techniques. MRI and histological correlation serves as quantitative morphology of skin structures including the epidermis, dermis layers and hair follicle. MRI is a powerful research tool with potential in dermatology and skin toxicology or pharmacotherapeutic monitoring.

Acknowledgments

The author thanks Dr. Mandip Sachdeva for providing fresh rat skin tissues and for the use of his ACUC protocol. The author also acknowledges the assistance of Dr. Bruce R. Locke for his generous help in manuscript correction and suggestions. The assistance of Dr. Suniket Fulzele, Kiran Shetty, Ashley Blue and Dr. William Brey from the National High Magnetic Field Laboratory, Tallahassee, FL, was valuable.

References

- [1] Fu R, Brey WW, Shetty K, Gor'kov P, Saha S, Long JR, et al. Ultra-wide bore 900 MHz high-resolution NMR at the National High Magnetic Field Laboratory. *J Mag Reson* 2005;177:1–8.
- [2] Keshvari J, Lang S. Comparison of radio frequency energy absorption in ear and eye region of children and adults at 900, 1800 and 2450 MHz. *Phys Med Biol* 2005;50(18):4355–69.
- [3] Narayanasamy K, Kandimala K, Lamba SS, et al. Structure–activity relationship of penetration enhancers in transdermal drug delivery. *Curr Med Chem* 2000;7:593–608.
- [4] Weis J, Astrom G, Vinnars B, et al. Chemical-shift micro-imaging of subcutaneous lesions. *MAGMA* 2005;18(2):59–62.
- [5] Yeung HN, Aisen AM. Magnetization transfer contrast with periodic pulsed saturation. *Radiology* 1992;183:209–14.
- [6] Yeung HN. On the treatment of transient response of a heterogeneous spin system to selective RF saturation. *Magn Reson Med* 1993;30:146–7.
- [7] Ceckler TL, Balaban RS. Field dispersion in water-macromolecular proton magnetization transfer. *J Magn Reson Ser B* 1994;105:242–8.
- [8] Natt O, Watanabe T, Boretius S, et al. Magnetization transfer MRI of mouse brain reveals areas of high neural density. *Magn Reson Imaging* 2003;21:1113–20.
- [9] Ablett S, Burdett N, Carpenter A, et al. Short echo time MRI enables visualisation of the natural state of human stratum corneum water in-vivo. *Magn Reson Imaging* 1996;14:357–60.
- [10] Richard S, Querleux B, Bittoun J, et al. In vivo proton relaxation times analysis of the skin layers by magnetic resonance imaging. *J Invest Dermatol* 1991;97(1):120–5.
- [11] Bittoun J, Saint-James H, Querleux BG, et al. In-vivo high-resolution MR imaging of the skin in a whole-body system at 1.5 T. *Radiology* 1990;176:457–60.
- [12] Hennig J, Scheffler K. Hyperechoes. *Magn Reson Med* 2001;46:6–12.
- [13] Hanley K, Jiang Y, Holleran WM, et al. Glucosylceramide metabolism. *J Lipid Res* 1997;38:576–84.
- [14] Kanikkannan N, Locke BR, Singh M. Effect of jet fuels on the skin morphology and irritation in hairless rats. *Toxicology* 2002;175(1–3):35–47.
- [15] Zemtsov A. Magnetic resonance in dermatology. *Arch Dermatol* 1993;129:215–6.
- [16] Wolff SD, Balaban RS. Magnetization transfer contrast (MTC) and tissue water proton relaxation in-vivo. *Magn Reson Med* 1989;10:135–44.
- [17] Grad J, Mendelson D, Hyder F, et al. Direct measurement of longitudinal relaxation and magnetization transfer in heterogeneous system. *J Magn Reson* 1990;86:416–9.
- [18] Wolff SD, Eng J, Balaban RS. Magnetization transfer contrast: method for improving contrast in gradient recalled-echo images. *Radiology* 1991;179:133–7.
- [19] Hu BS, Conolly SM, Wright GA, et al. Pulsed saturation transfer contrasts. *Magn Reson Med* 1992;26:231–40.
- [20] Jones RA, Southon TE. Improving the contrast in rapid imaging sequences with pulsed magnetization transfer contrast. *J Magn Reson* 1992;97:171–6.
- [21] Zhu XP, Hutchinson CE, Chilvers PB, et al. Off-resonance binomial composite pulses in 2D and 3D fat/water imaging at 0.5 T. *Br J Radiol* 1995;68(806):134–40.
- [22] Kovanlikaya A, Guclu C, Desai C, et al. Fat quantification using three-point Dixon technique: in vitro validation. *Acad Radiol* 2005;12(5):636–9.
- [23] Salvado O, Hillenbrand C, Zhang S, Wilson DL. Method to correct intensity inhomogeneity in MR images for atherosclerosis characterization. *IEEE Trans Med Imag* 2006;25(5):539–52.
- [24] Cheng H, Huang F. Magnetic resonance imaging image intensity correction with extrapolation and adaptive smoothing. *Magn Reson Med* 2006;55(4):959–66.
- [25] Dieter G. MicroImaging Manual: PARAVISION User Manual Version 006, vol. 6. Rheinstetten, Germany: Bruker Biospin; 2004. p. 187–208. DWG-Nr: 1429001.
- [26] Breen D, Whitaker R, Museth K, et al. Level set segmentation of biological volume datasets. In: Suri JS, Wilson DL, Laxminarayana S, editors. Hand book of biomedical image analysis. Volume 1: Segmentation models part 1, 1(1). New York: Kluwer Academic/Plenum Publishers030648550-8; 2005. p. 415–78.
- [27] Sharma R. MRI in carotid artery atherosclerosis plaque characterization. *Magn Reson Med Sci* 2002;1(4):217–32.
- [28] Kiessling F, Le-Huu M, Kunert T, et al. Improved correlation of histological data with DCE MRI parameter maps by 3D reconstruction,

- reslicing and parameterization of the histological images. *Eur Radiol* 2005;15:1079–86.
- [29] Hajnal JV, Baudouin CJ, Oatridge A, et al. Design and implementation of magnetization transfer pulse sequences for clinical use. *J Comput Assist Tomogr* 1992;16(1):7–18.
- [30] Ropele S, Siegfried SS, Augustin M, et al. A comparison of magnetization transfer ratio, magnetization transfer rate, and the native relaxation time of water protons related to relapsing-remitting multiple sclerosis. *Am J Neuroradiol* 2000;21:1885–91.
- [31] Song HK, Wehrli FW, Ma J. In-vivo MR microscopy of the human skin. *Magn Reson Med* 1997;37:185–91.
- [32] Jeong EK, Kim SE, Guo J, et al. High resolution DTI with 2D interleaved multislice reduced FOV single-shot diffusion weighted EPI(2D ss-rFOV-DWEPI). *Magn Reson Med* 2005;54:1575–9.
- [33] Dixon TW, Engels H, Castillo M, et al. Incidental magnetization transfer contrast in standard multislice imaging. *Magn Reson Imaging* 1990;8:417–22.